

Evolution of surface roughness of AlN and GaN induced by inductively coupled Cl₂/Ar plasma etching

K. Zhu, V. Kuryatkov, B. Borisov, J. Yun, G. Kipshidze, S. A. Nikishin, and H. Temkin
Department of Electrical Engineering, Texas Tech University, Lubbock, Texas 79409-3102

D. Aurongzeb and M. Holtz^{a)}
Department of Physics, Texas Tech University, Lubbock, Texas 79409-1051

(Received 24 September 2003; accepted 2 February 2004)

We study the effects of plasma etching on the evolution of surface roughness of GaN and AlN. The etch-induced roughness is investigated using atomic force microscopy by systematically varying plasma power, chamber pressure, and Cl₂/Ar mixture gas composition. GaN etches three to four times more rapidly than AlN for identical plasma conditions. For both GaN and AlN, we find that the surface roughness is correlated to etch rate. Induced roughness remains comparable to the as-grown value provided etching is carried out below rates 400 (GaN) and 90 nm/min (AlN). Above these cutoff etch rates, the roughness increases in proportion to etch rate. This result is independent of plasma parameters varied to produce the higher etching rates. By analyzing the surface properties through the power spectral density (PSD), we correlate roughness with the formation of fine-scale features present as a consequence of more aggressive etching. The cutoff etch rates and spatial-frequency dependence of the PSD are interpreted using the theory of kinetic roughening. A low-frequency range exhibits saturation corresponding to large-scale feature sizes, and a high-frequency regime exhibits scaling properties. © 2004 American Institute of Physics.
 [DOI: 10.1063/1.1688993]

I. INTRODUCTION

Principal metrics which are important in plasma etching are removal rate, anisotropy, selectivity, and etch surface properties. High-density plasma techniques result in high etch rates.^{1–5} However, plasma etching for device preparation must be optimized for anisotropy, selectivity, and etch-induced surface roughness. Surface roughness plays an important role in device performance,^{6–8} through increased contact resistance and surface-related carrier recombination. Despite this importance, there are very few reports focusing on etching-induced surface properties of the III-nitrides,^{9–11} and none focusing on AlN.

III-nitrides GaN and AlN, and their ternary alloys, are important materials for ultraviolet optoelectronics and high-temperature transistors. Because of their chemical stability, conventional wet etching is unsuitable for device processing. Plasma or dry etching is the preferred etching method, with a myriad of techniques including reactive ion etching (RIE),^{12–14} electron cyclotron resonance,^{15,16} chemical assisted ion-beam etching,^{17–19} magnetron RIE,^{20,21} and inductively coupled plasma (ICP).^{1,2,22,23} Inductively coupled plasma reactive ion etching (ICP-RIE) is the most popular among these techniques because it provides a high-density plasma and independently controlled substrate bias voltage. The chlorides of Ga, Al, and N are relatively volatile,^{3,15,24} making Cl₂, BCl₃, and SiCl₄ the primary reagents used to etch III-N group materials.

Previous etch studies have employed the theory of kinetic roughening to interpret surface properties^{25–28} includ-

ing a nonlinear term describing local etching.²⁹ Here, the time evolution of the surface $h(\mathbf{r}, t)$ is described by the nonlinear differential equation²⁵

$$\partial h / \partial t = \nu_{\text{des}} \nabla^2 h - \frac{\lambda}{2} (\nabla h)^2 - \kappa \nabla^4 h + \eta + \Phi_0, \quad (1)$$

where the two-dimensional vector $\mathbf{r} = (x, y)$ locates the in-plane coordinate and h is the third dimension. Φ_0 is independent of \mathbf{r} and takes into account uniform material flux leaving the etching surface. $\eta(\mathbf{r}, t)$ is a function which accounts for random processes at the etch surface. Conceptually, η can be decomposed into a term stemming from stochastic variation in the adsorption and desorption fluxes plus a term describing redistribution at the surface. In the case of plasma etching, the first and third terms on the right-hand side of Eq. (1) are influenced by effects related to variations in the etch rate due to surface desorption and redistribution of an etchant.²⁵ These terms are generally associated with smoothing. Due to their higher attack cross section under RIE,³⁰ etchant arriving on elevated features will tend to redistribute into existing crevices and that arriving in surface depressions will have a propensity to remain adsorbed. The effect of redirection is elevated concentration of etchant in local crevices. Consequently, the curvature terms [one and three in Eq. (1)] can be associated with a roughening phenomena. The second term in Eq. (1) attempts to account for the etching of surface features for which the *local* normal is not parallel to the global normal.²⁹ Coefficient λ is generally approximated by the vertical etch rate.

^{a)}Electronic mail: mark.holtz@ttu.edu

The influence of this nonlinear term in Eq. (1) is to enhance roughening. Thus, at a low etch rate, we expect the nonlinear term to diminish in importance, thus reducing Eq. (1) to the so-called Edwards–Wilkinson equation.³¹ Under high etch rate conditions, the roughening term is expected to grow in relative importance.

In this article, we report systematic studies of the relationships of etch rate and surface roughness on etching parameters. For these studies, we etch GaN and AlN using Cl₂/Ar plasma. The surface properties are studied using atomic force microscopy (AFM). Section III shows our results demonstrating a controlled etch process. Postetch surface properties are examined as a function of plasma parameters. We examine the effect of plasma etching parameters on surface roughness, and find a direct correlation between roughness and etch rate. The etched surfaces are further studied using the power spectral density of the AFM image, as discussed in Sec. IV. We analyze the results using the theory of kinetic roughening.

II. EXPERIMENTAL DETAILS

The GaN and AlN thin films used as starting material in this study were grown by gas-source molecular-beam epitaxy on silicon substrates.^{32–35} The original thickness of GaN and AlN epilayers were determined by the Fabry–Perot fringes in the optical reflectance spectrum³⁶ to be 1.0 μm and 0.7 μm, respectively. All measurements reported here are on nominally undoped materials. AlN wafers were examined with and without protective cap layers of GaN. Those grown with the cap layer were found to etch with no delay upon plasma processing, while those terminated with AlN showed a delay in the onset of etching. Our etch rate measurements come from AlN capped with ~5 nm of GaN to minimize the impact of this delay on etch rates obtained. Nickel was used to protect regions of the III-N layers during etching. The nickel was deposited using electron-beam evaporation and patterned using standard metal lift-off lithography. After etching, the Ni is removed, using either 37% HCl acid at 50–60 °C or a solution of HNO₃ and HF (10:1) at room temperature.

The etching was conducted in a commercial ICP-RIE plasma etch system. The etching was investigated as a function of ICP power, RIE power, Cl₂/Ar gas composition, and pressure in the chamber. The Cl₂/Ar mixture was distributed through a showerhead positioned 100 mm above the etching surface. A high-density ICP plasma discharge is generated by applying rf (13.56 MHz) power to the water-cooled inductive coil. The wafer electrode is powered by a 600 W rf generator also operated at 13.56 MHz. Because ion energy and plasma density are effectively decoupled for the ICP-RIE system, uniform density and energy distributions are transferred to the sample while keeping ion and electron energy low.³⁷ During the etching processes, the substrate was clamped to the electrostatic chuck with helium gas flowing on the wafer back side for cooling. The basic etching conditions are summarized in Table I. Holding each of the other parameters fixed, we systematically vary each parameter in turn to study its role in etching. The etch duration was 60 s. Scanning

TABLE I. Basic etching conditions.

Plasma Parameter	Value
ICP power	300 W
RIE power	150 W
Chamber pressure	8 mTorr
Cl ₂ /Ar flow rates	20/5 sccm

electron microscopy cross sections revealed all etching to be anisotropic. The etch step height was determined using a stylus profilometer. Surface properties were studied using AFM operated in contact mode. Surface properties are quantified using the root-mean-square (rms) surface roughness σ qualified over a range of 10×10 μm² area using

$$\sigma^2 = \frac{\sum_{i,j=1}^{N,M} (h_{i,j} - \bar{h})^2}{(N-1)(M-1)}, \quad (2)$$

where $h_{i,j}$ is the height at $\mathbf{r}=(x,y)$ coordinate denoted (i,j) and \bar{h} is the average surface height.

III. ETCHING PROPERTIES OF GaN AND AlN

In this section, we present our results on etch rate and surface roughness for GaN and AlN. AFM images of the GaN and AlN surfaces are shown in Figs. 1 and 2, respec-

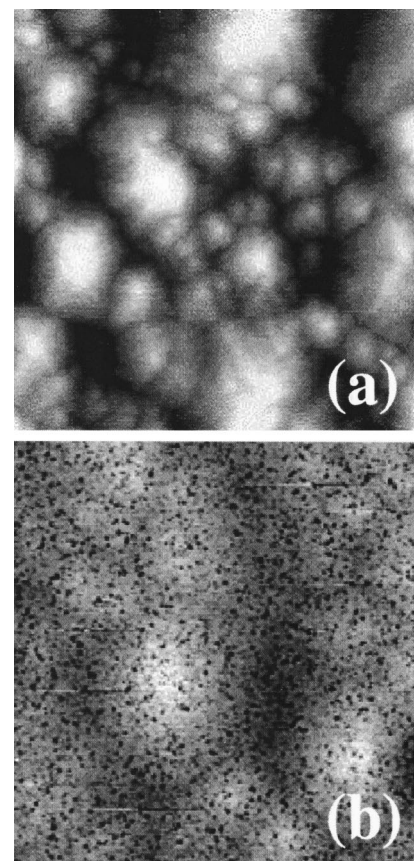


FIG. 1. 10 μm×10 μm AFM images of as-grown GaN (a) and following etching under the basic conditions (b). Note that the large-scale features in the as-grown layer are present following etching, with fine-scale roughness superimposed. The rms roughness values are 5.1 nm and 9.3 nm for (a) and (b), respectively.

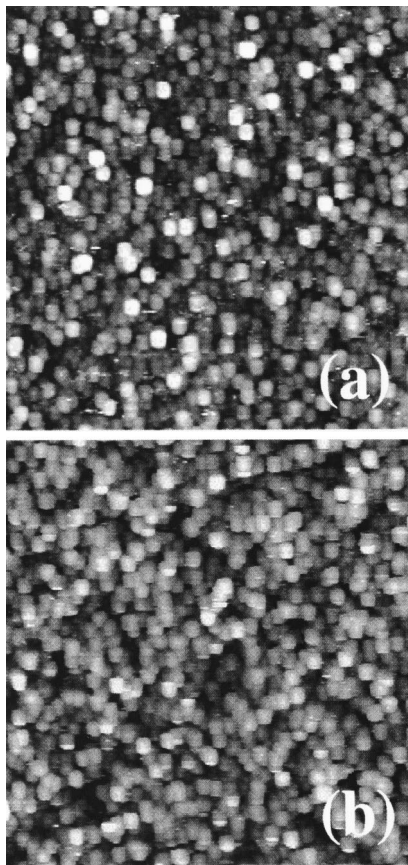


FIG. 2. $10\ \mu\text{m}\times 10\ \mu\text{m}$ AFM images of as-grown AlN (a) and following etching under the basic conditions (b). The rms roughness values are 6.3 nm and 19.3 nm for (a) and (b), respectively.

tively. For illustration, we show images of as-grown material subsequent to etching under the basic conditions in Table I. From these images in Figs. 1 and 2, we obtain area surface properties as a function of etch conditions. The relatively large features in Fig. 1, with sizes ranging from ~ 1 to $4\ \mu\text{m}$ across, are single-crystal grains surrounded by threading dislocation walls. The predominantly hexagonal shape of these grains supports this interpretation. The corresponding grain (or dislocation) density is on the order of $10^8\text{--}10^9\ \text{cm}^{-2}$, characteristic of GaN layers^{38–40} and in agreement with our x-ray diffraction measurements.⁴¹ As etch conditions change, the surface develops fine-scale ($<0.1\ \mu\text{m}$) lateral features and exhibits greater rms roughness.

The AlN surfaces show the small-scale surface roughness (Fig. 2). The lateral length scale, $\sim 0.2\ \mu\text{m}$, is consistent with typical crystal grain size in AlN epitaxial layers and with transmission electron microscopy of our materials.⁴² AlN etches slower than GaN, for identical conditions, due to the greater bond strength of AlN and its higher dielectric constant. As we will show, greater surface roughness correlates with higher etching rates.

In Figs. 3 and 4, we summarize the etch rate and rms surface roughness measurements for GaN and AlN, respectively. In each figure, we show rms roughness and etch rate together as a function of plasma parameters. We note two general points. First, GaN etches three to four times faster

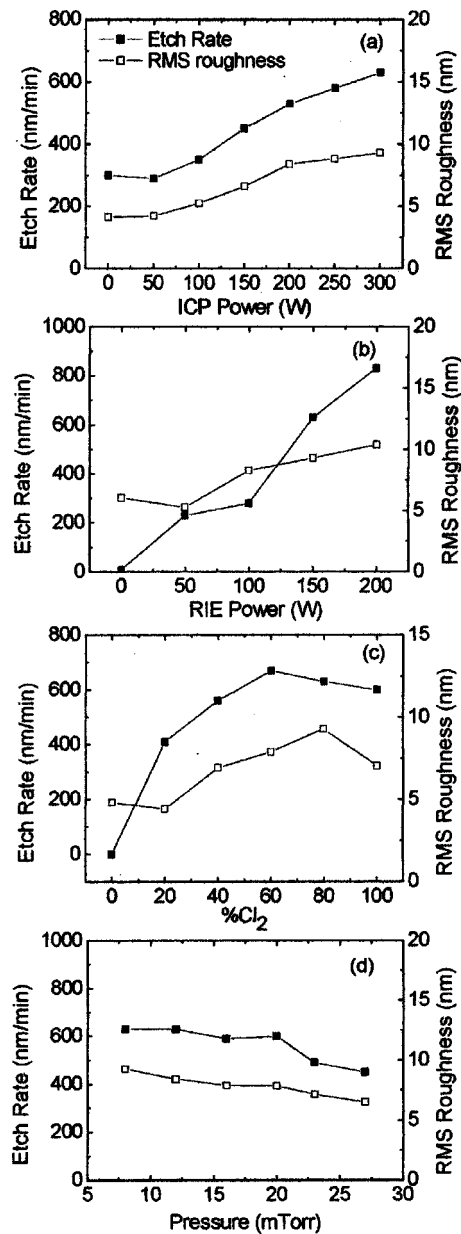


FIG. 3. GaN etch rates and rms roughness values as a function of plasma processing parameters. Typical experimental uncertainties in the etch rate are $\pm 10\ \text{nm/min}$. A maximum 10% variation is seen in the rms roughness across the samples.

than the AlN. Second, the roughness generally mimics the etch rate dependences. We discuss this point later.

Figures 3(a) and 4(a) show the etch rate and surface rms roughness as a function of ICP power. In Fig. 3(a) for GaN, when the ICP power increased from 0 to 300 W, the etch rate rose from 300 to 630 nm/min and the rms roughness increased accordingly from 4 nm to 9 nm. Figure 4(a) shows an AlN etch rate of 5 nm/min, at zero ICP power, gradually rising to 170 nm/min at 300 W. Over this same range, the roughness has also an increasing trend. Increased ICP power produces more reactive ions and neutrals, which in turn elevates the etch rate.^{2,37,43} The roughness measurements imply that surface roughness is correlated to etch rate. Despite the lower etch rate of AlN, the rms roughness values are higher than those of GaN. It should be noted that the as-

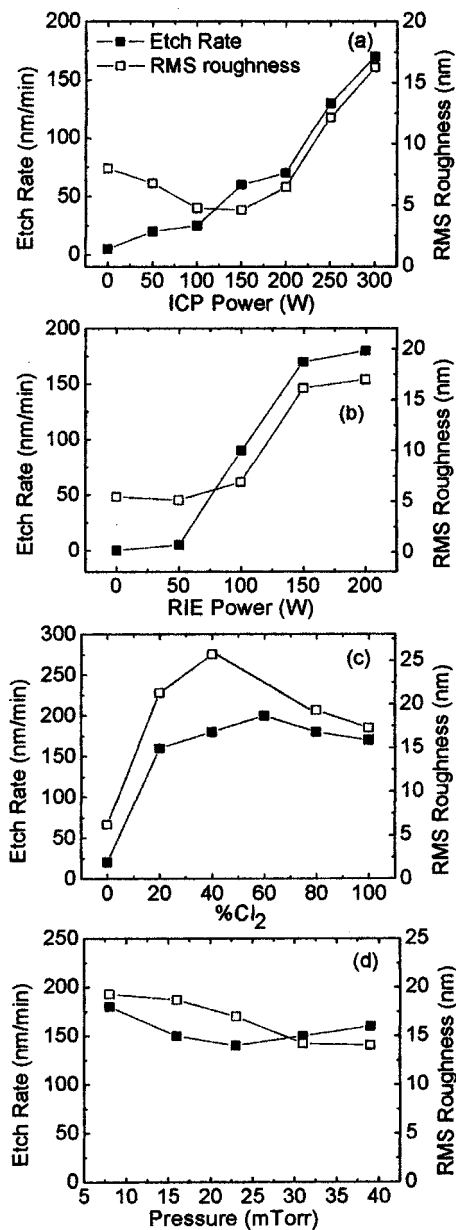


FIG. 4. AIN etch rates and rms roughness values as a function of plasma processing parameters. Experimental uncertainties are the same as in Fig. 3.

grown AIN had a slightly higher roughness than that of GaN, 6.3 nm compared to 4.5 nm. In Fig. 4(a), we even see a slight reduction in rms roughness with ICP power, possibly due to smoothing effects of the etch as discussed in regard to Eq. (1).

Figures 3(b) and 4(b) show the surface roughness and etch rate as functions of RIE power. In Fig. 3(b), the GaN etch rate rises from zero to 830 nm/min as RIE power is increased from zero to 200 W. For AIN, shown in Fig. 4(b), the etch rate increases from zero to 180 nm/min, over the same power range, and the roughness increases from the as-grown value to 17 nm. The sensitivity of etch rate to RIE power stems from the effectiveness of surface sputtering, which improves removal of etch byproducts and assists in bond breaking.^{24,44} We expect the roughness to also increase due to surface sputtering, as is seen more clearly in the case

of AIN. For AIN, a relationship is clearly seen between etch rate and roughness in Fig. 4(b).

Figures 3(c) and 4(c) show the dependence of etch rate and rms roughness on the gas composition. The total Cl₂ and Ar gas flow rate was held constant at 25 sccm, and the percent of Cl₂ composition varied from 0 to 100%. GaN and AIN etch rates exhibit similar profiles, increasing in the low Cl₂ fraction range, reaching maxima near 60%. Two factors contribute to the observed trend. First, since chlorine radicals are responsible for the chemical etching, increasing the Cl₂ component of the gas composition will raise the etch rate.^{3,23,45} This explains the increasing trend at low Cl₂ composition. Second, argon contributes to efficient decomposition and ionization of the chlorine feed gas and, more importantly for RIE, plays the primary role in removing the etch byproducts. Etch byproducts remaining on the surface block fresh etchant from arriving, explaining the saturation and eventual reduction seen in the etch rates at high Cl₂ composition. Both Cl₂ and Ar are necessary for achieving high etch rates and a mixture is more effective than either pure Cl₂ or pure Ar. The observed surface roughness trend is similar to the etch rate trend for both GaN and AIN, with analogous explanation. At low Cl₂ gas composition, etching is not sufficiently aggressive to roughen the surface. As the argon content rises, the surface receives commensurately higher physical (sputtering) damage. With only Cl₂ gas as an etchant, the surface damage is reduced as a balance is achieved between high chlorine radical concentration and protection of the surface by etch byproducts.

Figures 3(d) and 4(d) show the dependence of etch rate and surface roughness on gas pressure. The gas pressure was varied from 8 to 27 mTorr for the GaN studies, and from 8 to 39 mTorr for AIN etching. This is regarded as the low-pressure etching regime. The GaN etch rate gradually slows over the pressure range studied, decreasing from 620 to 470 nm/min. A higher etch rate, which reduces with pressure, was reported for GaN etching below 7 mTorr.^{1,21} The AIN exhibits a flat dependence. Chamber pressures in this range clearly play the weakest role in determining etch rates and roughness, in comparison to the other parameters studied. Increasing the gas pressure reduces the mean-free path as well as the plasma efficiency and sputtering on the etch surface. This is consistent with mass spectrometry studies of etching products, in which a decrease in GaCl_x was observed as the gas pressure increased from 0.25 to 2 mTorr.⁴⁶

IV. CORRELATION BETWEEN ETCH RATE AND ETCHING-INDUCED SURFACE ROUGHNESS

In each of the cases summarized in Figs. 3 and 4, we note a correlation between etch rate and induced surface roughness. We substantiate this relationship in Fig. 5, where we graph surface roughness versus etch rate for GaN [Fig. 5(a)] and AIN [Fig. 5(b)]. The results show the rms roughness to remain near the as-grown value to etch rates of 400 nm/min for GaN, Fig. 5(a), then rise at a slope of about ~ 0.016 min. In Fig. 5(b), the AIN roughness remains close to the as-grown surface up to an etch rate of 90 nm/min, above which it rises at the much higher slope ~ 0.15 min. Based on induced roughness, we determine the desired etch

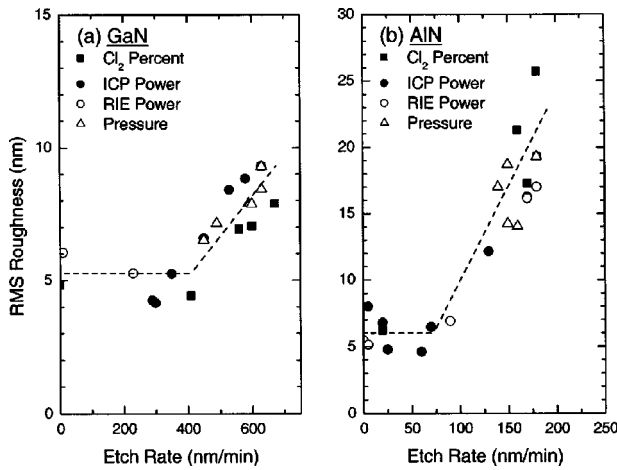


FIG. 5. rms roughness as a function of etch rate. (a) GaN and (b) AlN. Note the different scales for these two panels. The rms roughness has maximum variation of 10%, the etch rates are accurate to ± 10 nm/min.

rate for GaN and AlN to be 400 nm/min and 90 nm/min, respectively. Etching parameters producing material removal below these rates are expected to provide surfaces without causing additional roughening. Above these etch rates the induced roughness rises. We conclude that a more aggressive etch will produce a rougher surface. From the AFM images, the increase in rms roughness is associated with the emergence of fine-scale features. The higher slope seen for AlN in Fig. 5(b), and the corresponding onset of roughening at lower etch rate, are attributed to the fine-scale features which are due to growth. These features make the surface more susceptible to local etching.

For low density etching, the average ion spacing d_{etchant} is on the order of the crystalline grain sizes $d_{\text{etchant}} \approx L_{\text{AlN}} < L_{\text{GaN}} < \langle l \rangle$, where L_{AlN} and L_{GaN} are the lateral feature sizes on the surface and $\langle l \rangle$ is the mean-free path in the plasma. Low etchant ion flux results in little competition for available surface area, and smooth surfaces etch slowly without extensive roughening. As the flux increases, the situation at the etch surface changes. Competition for etching sites at the surface will favor redistribution into crevices, a process enhanced by ion bombardment under RIE. Due to the lower attack cross section of crevices under RIE,³⁰ the etchant arriving on elevated features will tend to redistribute into existing crevices and that arriving in surface depressions will have a propensity to remain adsorbed. The result is an elevated concentration of etchant in crevices producing locally higher etch rates in comparison to higher-lying features.

The dependence illustrated in Fig. 5 is qualitatively consistent with what is expected from Eq. (1) for varying etch rates. At a low etch rate, we expect the nonlinear (local) etching term to be less important than at high removal rate, for which redistribution into crevices is favored. We thus obtain a cutoff etch rate, below which the Edwards–Wilkinson description of the surface evolution is valid and above which the nonlinear Kardar–Parisi–Zhang term must be taken into account. The nonlinear term in Eq. (1) is expected to play a dominant role when the roughness $\sigma \geq 2\nu_{\text{des}}/\lambda$. In the case of Cl_2 etching of GaAs, this value was found to be ~ 10 nm.²⁶ In our case, the corresponding

roughness is ≥ 5 nm for both GaN and AlN. Associating λ with the lowest etch rates at which the nonlinear term in Eq. (1) becomes important for GaN (400 nm/min) and AlN (90 nm/min), we estimate corresponding values of ν_{des} to be 1000 and 230 nm²/min. These values are higher than those reported for thermal Cl_2 etching of GaAs, ~ 120 (Ref. 25) and 240 nm²/min.²⁶ However, since the desorption coefficient is proportional to flux at the surface,⁴⁷ it will be influenced by surface bombardment under RIE.

In addition to the rms roughness, we also analyze the AFM surface data using the measured height correlation function $G(\rho, t) = \langle [h(\mathbf{r}_1, t) - h(\mathbf{r}_2, t)]^2 \rangle$, with $\rho = |\mathbf{r}_2 - \mathbf{r}_1|$. This often exhibits scaling (power) laws such that $G(\rho, t) \sim \rho^\alpha$ at fixed time. $h(\mathbf{r}, t)$ is the same height function as in Eq. (1), α is the scaling parameter. This scaling behavior is interpreted using the theory of kinetic roughening. Averaging in the expression for $G(\rho, t)$ is formally accomplished by using all possible choices of origin. Equivalently,⁴⁸ the PSD can be used to examine the scaling dependence. In one dimension,⁴⁹ the PSD is calculated using

$$\text{PSD}(k) = \left[\int h(x) e^{ikx} dx \right]^2, \tag{3}$$

where k corresponds to the spatial frequency. As in Ref. 49, we analyzed the AFM image by generating the Fourier transform for individual data columns then multiplying the transform by its complex conjugate. These are then averaged to produce the final PSD. The valid spatial frequency range is determined in practice by the AFM scan length ($L_{\text{scan}} = 10 \mu\text{m}$) and AFM tip radius ($R_{\text{tip}} \sim 10$ nm), such that $10/L_{\text{scan}} \leq k \leq 1/R_{\text{tip}}$. The PSD can then be used to extract the scaling behavior according to

$$\text{PSD}(k) \propto k^{-\gamma} \tag{4}$$

where the exponent γ is related to height correlation function exponent through $\alpha = (\gamma - d)/2$ (Ref. 48) and the fractal scaling exponent is $3 - \alpha/2$.⁵⁰ For the one-dimensional line scan analysis method used here, $d = 1$.

Figure 6 shows representative PSD spectra for GaN etched under various RIE etch powers, corresponding to Fig. 3(b). The PSD from an analysis of the as-grown AlN is also shown in Fig. 6. Focusing first on the GaN, a low-frequency saturation range is seen corresponding to desorption-dominated behavior. This is followed by a scaling range over which the PSD decreases, as in Eq. (4). The transition seen in the dependence of the PSD occurs at a cutoff value k_c , corresponding to scaling length $\rho_c = 1/k_c$. The surface is essentially flat according to measurements on the $k < k_c$ scale. ρ_c corresponds to the crystal grains seen in the AFM images. Two trends are clear in Fig. 6. First, the cutoff k_c between the low-frequency saturation and the scaling ranges moves to higher spatial frequency with higher RIE etch power. From Figs. 3 and 5, this corresponds to greater etch rate and roughness. Second, the slope of the scaling regime (exponent) is seen to slightly decrease. A PSD surface analysis of images obtained varying the other etch parameters shows that conditions which roughen the sample surface produce a decrease in ρ_c . This is consistent with the elevated roughening seen

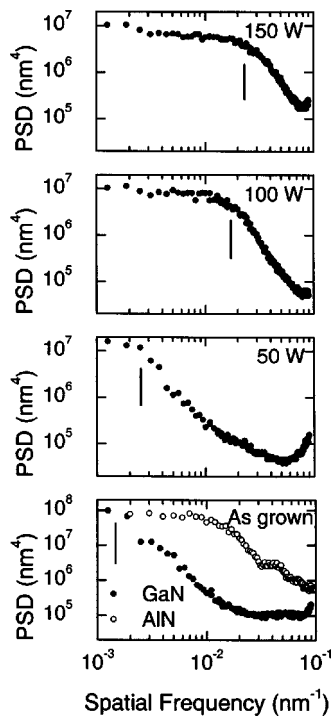


FIG. 6. Power spectral density vs spatial frequency for GaN (filled symbols) etched under various RIE powers. Dashed lines are fits over the scaling range. The solid vertical lines demarcate the transition from scaling to saturation, k_c (note $\rho_c = 1/k_c$). The PSD for as-grown AlN is shown in the lower panel (open symbols).

from the rms roughness data. Trends seen in α are not as pronounced, indicating perhaps that the lateral scaling is coupled to the etching parameters. As pointed out in Ref. 51, the roughness exponent is not a measure of roughness itself, although the cutoff length appears to be useful in characterizing the nature of roughness. Further investigations are required to establish the interaction between etching conditions and scaling, particularly under combined ICP and RIE etching.

Robey²⁵ examined surface properties of GaAs following rf etching in a Cl_2/H_2 plasma with pressures and rf powers on the order of what we use here, although the temperature was elevated to 380 °C and efforts were taken to minimize surface bombardment. A value of $\rho_c \sim 30$ nm was reported. Schmid and co-workers²⁶ also etched GaAs using thermal Cl_2 with the substrate at 200 °C. Their PSD analysis of postetch AFM surface properties show a rounded dependence, with transition from a low- to high-slope regime occurring between 20 and 100 nm. Finally, Zhao *et al.*²⁷ examined the etch properties of Si using CF_4/O_2 with plasma power 102 W and at a somewhat higher processing pressure of 300 mTorr and varying time. For comparable etch depths, the scaling length observed was ~ 50 nm. Robey^{25,29} interpreted the critical length scale in terms of the parameters of Eq. (1) according to $\rho_c = 2\pi\sqrt{\kappa/\nu_{\text{des}}}$. In Fig. 6, we see that k_c increases with higher RIE power, corresponding to a decrease in ρ_c from ~ 600 to 40 nm. We attribute this trend to elevated desorption frequency ν_{des} with increasing surface bombardment due to the RIE, although we also expect parameter κ to depend on plasma conditions, such as RIE

power. From our limited data set, we observe an RIE power dependence consistent with $\rho_c \propto 1/\sqrt{P}$. For GaN, we see the general trend of diminishing scaling length with increasing roughness and etch removal rate. The greater rms roughness is related to smaller feature sizes, which in turn enhance local etching described by the nonlinear term in Eq. (1). At the etch rates in Fig. 5(a), where GaN roughness begins to grow, we use the values of ρ_c obtained from the PSD analysis and our estimate of ν_{des} discussed above to obtain $\kappa \leq 23\,000$ nm⁴/min. This value is comparable to the value of 36 000 nm⁴/min reported for Cl_2 etching of GaAs.²⁶

The scaling exponents obtained from the PSD analysis of the GaN surface data range from ~ 0.10 to 1.10. The uncertainty in α is below ± 0.10 in all cases. In the case of thermal Cl_2 etching of GaAs, exponents group into two ranges: 0.1–0.2 and 0.7–0.8.²⁵ In Ref. 26, also concerning thermal Cl_2 etching of GaAs, a rounded dependence was seen on the PSD function, with α starting ~ 1 at high k then reducing to saturation with decreasing spatial frequency. Plasma etching of Si produced an exponent within experimental error of unity.²⁷

For the PSD analysis of as-grown and etched AlN, the surface features are small, and we also observe two scaling exponents, with a transition at small $\rho_c \sim 100$ nm (Fig. 6). This corresponds to the typical feature sizes seen in the AFM images. The exponent found at higher- k ranges from 0.40 to 1.06 which is generally higher than those of GaN. The as-grown AlN surfaces examined have a scaling exponent from 0.65 to 0.76. Uncertainty obtained in α from analyzing individual AFM images is better than ± 0.10 . We note a weak shoulder near $k = 0.04$ nm⁻¹ which we attribute to the 20 to 50 nm features generally seen in the AFM images of AlN. The AlN surface differs from that of the GaN because it has initial lateral surface properties similar to the fine-scale roughness produced by the etching process. Thus, the PSD analysis shows that the low-spatial frequency as-grown features exhibit little or no scaling dependence, while at higher spatial frequency there is evidence for scaling with an exponent varying near that of the as-grown surface. We conclude that the etch conditions used here generally retain the in-plane spatial features, but enhance the roughness at high removal rates.

V. SUMMARY AND CONCLUSIONS

In summary, surface roughness of GaN and AlN etched by ICP-RIE Cl_2/Ar plasma has been systematically investigated as a function of plasma parameters. GaN is found to etch three to four times more rapidly than AlN under identical conditions. The experimental results show that the surface roughness is not substantially increased by etching below a certain rate. Beyond that etch rate, surface roughness is proportional to etch rate. This conclusion is independent of which process parameters are varied to increase the etch rate. For GaN, the maximum etch rate, above which surface roughness increases, is 400 nm/min [Fig. 5(a)]. For AlN, the corresponding maximum is 90 nm/min [Fig. 5(b)]. These experiments allow us to set upper bounds on desired etch rates, guiding etching conditions for device processing. The result

is interpreted using the theory of kinetic roughening through PSD spatial-frequency analysis of the surface height function. Results are shown in Fig. 6. We see two frequency ranges: the low spatial-frequency range shows little correlation, while the high-frequency regime exhibits scaling. The cutoff length between these two regimes depends on processing conditions, and is associated with the observed feature sizes. Increased rms roughness is associated with diminishing ρ_c , thus associating the roughness with the development of fine-scale features. The scaling exponents also vary with etching conditions, although we do not obtain a clear trend as with the simpler rms roughness statistical analysis. From the results in Figs. 5 and 6, we obtain estimates of the kinetic coefficients in Eq. (1). Although there are no published parameters for etching GaN or AlN, we find reasonable agreement with results reported for Cl₂ etching of GaAs.

ACKNOWLEDGMENTS

The authors acknowledge support from the NSF (ECS-0070240, ECS-0323640, ECS-0304224, and CTS-0210141), DARPA (Dr. J. Carrano), U.S. Army SBCCOM, NATO Science for Peace (974505), and the J. F Maddox Foundation.

- ¹R. J. Shul, G. B. McClellan, S. A. Casalnuovo, D. J. Rieger, S. J. Pearton, C. Constantine, C. Barratt, R. F. Karlicek, Jr., C. Tran, and M. Schurman, *Appl. Phys. Lett.* **69**, 1119 (1996).
- ²S. A. Smith, C. A. Wolden, M. D. Bremser, A. D. Hanser, R. F. Davis, and W. V. Lampert, *Appl. Phys. Lett.* **71**, 3631 (1997).
- ³Y. H. Lee, H. S. Kim, J. Y. Yeom, J. W. Lee, M. C. Yoo, and T. I. Kim, *J. Vac. Sci. Technol. A* **16**, 1478 (1998).
- ⁴C. B. Vartuli, S. J. Pearton, J. W. Lee, J. Hong, J. D. Mackenzie, C. R. Abernathy, and R. J. Shul, *Appl. Phys. Lett.* **69**, 1426 (1996).
- ⁵K. Zhu, V. Kuryatkov, B. Borisov, G. Kipshidze, S. A. Nikishin, H. Temkin, and M. Holtz, *Appl. Phys. Lett.* **81**, 4688 (2002).
- ⁶D. A. Francis, C. J. Chang-Hasnain, and K. Eason, *Appl. Phys. Lett.* **68**, 1598 (1996).
- ⁷M. V. Bazylenko, M. Gross, and M. Faith, *Appl. Phys. Lett.* **69**, 2178 (1996).
- ⁸B. Rong, E. V. D. Drift, R. J. Reeves, W. G. Sloof, and R. Cheung, *J. Vac. Sci. Technol. B* **19**, 2917 (2001).
- ⁹J. W. Lee, J. Hong, C. R. Abernathy, E. S. Lambers, S. J. Pearton, W. S. Hobson, and F. Ren, *J. Vac. Sci. Technol. B* **14**, 2567 (1996).
- ¹⁰Y. B. Hahn, R. J. Choi, J. H. Hong, H. J. Park, C. S. Choi, and H. J. Lee, *J. Appl. Phys.* **92**, 1189 (2002).
- ¹¹S. Tripathy, A. Ramam, S. J. Chua, J. S. Pan, and Alfred Huan, *J. Vac. Sci. Technol. A* **19**, 2522 (2001).
- ¹²M. E. Lin, Z. F. Fan, A. Ma, L. H. Allen, and H. Morkoc, *Appl. Phys. Lett.* **64**, 887 (1994).
- ¹³I. Adesida, A. Mahajan, E. Andideh, M. Asif Khan, D. T. Olasen, and J. N. Kuznia, *Appl. Phys. Lett.* **63**, 2777 (1993).
- ¹⁴H. Lee, D. B. Oberman, and J. S. Harris, *Appl. Phys. Lett.* **67**, 1754 (1995).
- ¹⁵S. J. Pearton, C. R. Abernathy, and F. Ren, *Appl. Phys. Lett.* **64**, 2294 (1994).
- ¹⁶S. J. Pearton, C. R. Abernathy, F. Ren, J. R. Lothian, P. W. Wisk, A. Katz, and C. Constantine, *Semicond. Sci. Technol.* **8**, 310 (1993).
- ¹⁷M. W. Geis, G. A. Lincoln, N. Efremow, and W. J. Piacentini, *J. Vac. Sci. Technol.* **19**, 1390 (1981).
- ¹⁸I. Adesida, A. T. Ping, C. Youtsey, T. Dow, M. Asif Khan, D. T. Olson, and J. N. Kuznia, *Appl. Phys. Lett.* **65**, 889 (1994).
- ¹⁹A. T. Ping, I. Adesida, and M. Asif Khan, *Appl. Phys. Lett.* **67**, 1250 (1995).
- ²⁰G. F. McLane, M. Meyyappan, H. S. Lee, M. W. Cole, D. W. Eckart, R. T. Lareau, M. Namaroff, and J. Sasserath, *J. Vac. Sci. Technol. B* **11**, 333 (1993).
- ²¹G. F. McLane, L. Casas, S. J. Pearton, and C. R. Abernathy, *Appl. Phys. Lett.* **66**, 3328 (1995).
- ²²R. J. Shul, R. D. Briggs, J. Han, S. J. Pearton, J. W. Lee, C. B. Vartuli, K. P. Kulleen, and M. J. Ludowise, *Mater. Res. Soc. Symp. Proc.* **486**, 355 (1997).
- ²³R. J. Shul, G. B. McClellan, R. D. Briggs, D. J. Rieger, S. J. Pearton, C. R. Abernathy, J. W. Lee, C. Constantine, and C. Barratt, *J. Vac. Sci. Technol. A* **15**, 633 (1997).
- ²⁴D. Basak, K. Yamashita, T. Sugahara, Q. Fareed, D. Nakagawa, K. Nishino, and S. Sakai, *Jpn. J. Appl. Phys., Part 1* **38**, 2646 (1999).
- ²⁵S. W. Robey, *Phys. Rev. B* **65**, 115306 (2002).
- ²⁶J. H. Schmid, A. Ballestad, B. J. Ruck, M. Adamczyk, and T. Tiedje, *Phys. Rev. B* **65**, 155315 (2002).
- ²⁷Y.-P. Zhao, J. Drotar, G.-C. Wang, and T.-M. Lu, *Phys. Rev. Lett.* **82**, 4882 (1999).
- ²⁸A. Iwamoto, T. Yoshinobu, and H. Iwasaki, *Phys. Rev. E* **59**, 5133 (1999).
- ²⁹M. Kardar, G. Parisi, and Y.-C. Zhang, *Phys. Rev. Lett.* **56**, 889 (1986).
- ³⁰J. Drotar, Y.-P. Zhao, T.-M. Lu, and G.-C. Wang, *Phys. Rev. B* **61**, 3012 (2000).
- ³¹S. G. Edwards and D. R. Wilkinson, *Proc. R. Soc. London, Ser. A* **381**, 17 (1982).
- ³²S. A. Nikishin, N. N. Faleev, V. G. Antipov, S. Francoeur, L. Grave de Peralta, G. A. Seryogin, H. Temkin, T. I. Prokofyeva, M. Holtz, and S. N. G. Chu, *Appl. Phys. Lett.* **75**, 2073 (1999).
- ³³S. A. Nikishin, V. G. Antipov, S. Francoeur, N. N. Faleev, G. A. Seryogin, V. A. Elyukhin, H. Temkin, T. I. Prokofyeva, M. Holtz, A. Konkar, and S. Zollner, *Appl. Phys. Lett.* **75**, 484 (1999).
- ³⁴S. Nikishin, N. N. Faleev, A. S. Zubrilov, V. G. Antipov, and H. Temkin, *Appl. Phys. Lett.* **76**, 2910 (2000).
- ³⁵M. Seon, T. Prokofyeva, M. Holtz, S. A. Nikishin, N. N. Faleev, and H. Temkin, *Appl. Phys. Lett.* **76**, 1842 (2000).
- ³⁶M. Holtz, T. Prokofyeva, M. Seon, K. Copeland, J. Vanbuskirk, S. Williams, S. Nikishin, V. Tretyakov, and H. Temkin, *J. Appl. Phys.* **89**, 7977 (2001).
- ³⁷S. J. Pearton, J. C. Zolper, R. J. Shul, and F. Ren, *J. Appl. Phys.* **86**, 1 (1999).
- ³⁸V. Bousquet, J. Heffernan, J. Barnes, and S. Hooper, *Appl. Phys. Lett.* **78**, 754 (2001).
- ³⁹D. J. Smith, D. Chandrasekhar, B. Sverdlov, A. Botchkarev, A. Salvador, and H. Morkoc, *Appl. Phys. Lett.* **67**, 1830 (1995).
- ⁴⁰I. Berishev, A. Bensaoula, I. Rusakova, A. Karabutov, M. Ugarov, and V. P. Ageev, *Appl. Phys. Lett.* **73**, 1808 (1998).
- ⁴¹S. A. Nikishin, N. N. Faleev, V. G. Antipov, S. Francoeur, L. Grave de Peralta, G. A. Seryogin, H. Temkin, T. Prokofyeva, M. Holtz, and S. N. G. Chu, *Appl. Phys. Lett.* **79**, 2073 (1999).
- ⁴²G. Kipshidze, V. Kuryatkov, B. Borisov, S. A. Nikishin, M. Holtz, S. N. G. Chu, and H. Temkin, *Phys. Status Solidi A* **192**, 286 (2002).
- ⁴³Hyun Cho, C. B. Vartuli, S. M. Donovan, C. R. Abernathy, S. J. Pearton, R. J. Shul, and C. Constantine, *J. Vac. Sci. Technol. A* **16**, 1631 (1998).
- ⁴⁴C. B. Vartuli, J. D. Mackenzie, J. W. Lee, C. R. Abernathy, S. J. Pearton, and R. J. Shul, *J. Appl. Phys.* **80**, 3705 (1996).
- ⁴⁵R. J. Shul, C. G. Willison, J. Han, J. W. Lee, S. J. Pearton, C. R. Abernathy, S. M. Donovan, L. Zhang, and L. F. Lester, *J. Vac. Sci. Technol. A* **16**, 1621 (1998).
- ⁴⁶C. R. Eddy, *MRS Internet J. Nitride Semicond. Res.* **4S1**, (1999).
- ⁴⁷C. N. Luse and A. Zangwill, *Phys. Rev. B* **48**, 1970 (1993).
- ⁴⁸J. Krug, *Adv. Phys.* **46**, 139 (1997).
- ⁴⁹A. E. Lita and J. E. Sanchez, *Phys. Rev. B* **61**, 7692 (2000).
- ⁵⁰G. Chan and A. T. A. Wood, *Statistical Sinica* **10**, 343 (2000).
- ⁵¹J. Krim and J. O. Indekeu, *Phys. Rev. E* **48**, 1576 (1993).